

Statistical properties of filaments in the cosmic web

Youcai Zhang^{1*}, Hong Guo¹, Xiaohu Yang^{2,3}, Peng Wang¹

¹*Shanghai Astronomical Observatory; Nandan Road 80, Shanghai 200030, China*

²*Tsung-Dao Lee Institute and Key Laboratory for Particle Physics, Astrophysics, and Cosmology, Ministry of Education, Shanghai Jiao Tong University, Shanghai 200240, China*

³*Department of Astronomy, School of Physics and Astronomy and Shanghai Key Laboratory for Particle Physics and Cosmology, Shanghai Jiao Tong University, Shanghai 200240, China*

August 7, 2024

ABSTRACT

In the context of the cosmological and constrained ELUCID simulation, this study explores the statistical characteristics of filaments within the cosmic web, focussing on aspects such as the distribution of filament lengths and their radial density profiles. Using the classification of the cosmic web environment through the Hessian matrix of the density field, our primary focus is on how cosmic structures react to the two variables R_s and λ_{th} . The findings show that the volume fractions of knots, filaments, sheets, and voids are highly influenced by the threshold parameter λ_{th} , with only a slight influence from the smoothing length R_s . The central axis of the cylindrical filament is pinpointed using the medial-axis thinning algorithm of the COWS method. It is observed that median filament lengths tend to increase as the smoothing lengths increase. Analysis of filament length functions at different values of R_s indicates a reduction in shorter filaments and an increase in longer filaments as R_s increases, peaking around $2.5R_s$. The study also shows that the radial density profiles of filaments are markedly affected by the parameters R_s and λ_{th} , showing a valley at approximately $2R_s$, with increases in the threshold leading to higher amplitudes of the density profile. Moreover, shorter filaments tend to have denser profiles than their longer counterparts.

Key words: large-scale structure of universe – methods: statistical – cosmology: observations

1 INTRODUCTION

On the order of Mpc scales, the distribution of galaxies and dark matter reveals a striking gigantic network named cosmic web (Bond et al. 1996) consisting of knots (or clusters), filaments, sheets (or walls) and voids, arising from the primordial density fluctuations via gravitational instability (Peebles 1967; Zel’dovich 1970). Filaments are highly intriguing features in the cosmic web and play an important role in matter transport as bridges between galaxies. The main challenges in the study of the cosmic web are to precisely identify the filamentary structures and quantitatively characterize the properties of filaments, such as the distribution of filament length and the profile of radial density (Galárraga-Espinosa et al. 2020; Pfeifer et al. 2022; Zakharova et al. 2023; Wang et al. 2024a).

In observation, cosmic filaments traced by galaxies are well drawn by galaxy redshift surveys, such as the Center for Astrophysics redshift survey (CfA, de Lapparent et al. 1986), the Sloan Digital Sky Survey (SDSS, Abazajian et al. 2009) and the Dark Energy Spectroscopic Instrument (DESI, DESI Collaboration et al. 2024). Furthermore, cosmological simulations have been performed to present the evolution of dark matter, which allows a more detailed study of filaments traced by the dark matter distribution (Springel et al. 2005; Zhang et al. 2009; Dubois et al. 2014; Wang et al. 2024b). Compared to approximately spherical structures, filaments are more complicated geometric structures associated with a distinct direction in

space, resulting in some challenges in identifying cosmic filaments based on galaxies in observation or dark matter particles in simulation (Zakharova et al. 2023).

Over recent decades, numerous methods have been formulated for the detection of cosmic filaments through geometric or topological evaluations of the discrete distributions of particles in simulations or observed galaxies (Stoica et al. 2005; Sousbie 2011; Sousbie et al. 2011; Chen et al. 2015; Bonnaire et al. 2020), including the analysis of the Hessian matrix of density, tidal, or velocity shear tensors (Colombi et al. 2000; Aragón-Calvo et al. 2007; Hahn et al. 2007; Forero-Romero et al. 2009; Hoffman et al. 2012; Cautun et al. 2013; Wang et al. 2020), and the application of machine learning approaches (Aragon-Calvo 2019; Buncher & Carrasco Kind 2020; Suárez-Pérez et al. 2021; Carrón Duque et al. 2022). A detailed comparison of the different filament finders is presented in Libeskind et al. (2018). In general, these filament detection algorithms are designed for different purposes in studies. Assessing the relative success of these methods is challenging because there is no universally accepted definition of filaments (Alina et al. 2022; Inoue et al. 2022; Zhang et al. 2022a; Aragon-Calvo 2024).

With the help of filament detection methods, several studies of cosmic filaments have been carried out to investigate the effects of the environment on galaxy formation and evolution (Kuutma et al. 2017; Chen et al. 2017). By applying the DisPerSE filament identification algorithm (Sousbie 2011) to galaxies at redshift $z \approx 0.7$ in the VIPERS survey, Malavasi et al. (2017) found that more massive or passive galaxies are closer to the filaments than less massive or ac-

* yczhang@shao.ac.cn

tive galaxies. Based on the filament catalogs traced by the DisPerSE algorithm, the lower specific star formation rates with decreasing distance to the filaments are also confirmed in the GAMA survey with $0.02 \leq z \leq 0.25$ (Kraljic et al. 2018), in the COSMOS with $0.5 < z < 0.9$ (Laigle et al. 2018), and in the SDSS with $z \sim 0.1$ (Winkel et al. 2021).

Recent studies have focused on the statistical properties of cosmic filaments, such as their lengths and radial density profiles (Malavasi et al. 2020; Yang et al. 2022; Galárraga-Espinosa et al. 2020, 2024). Observationally, using filament samples identified by the Smoothed Hessian Major Axis Filament Finder (SHMAFF) for SDSS ($z \sim 0.1$) and DEEP2 ($z \sim 0.8$), Bond et al. (2010) and Choi et al. (2010) discovered that the distribution of filament lengths is roughly exponential and that the filament widths are heavily influenced by the smoothing scales used in the creation of the smoothed density. Wang et al. (2024a) propose that filament radii should be identified at points where galaxy number density profiles have the minimal gradient around filaments. This approach provides a physical delineation of filament boundaries akin to the splashback radius observed in dark matter halos (Diemer & Kravtsov 2014). Using filaments traced by the DisPerSE algorithm for SDSS MGS and LOWZ+CMASS samples, Malavasi et al. (2020) examined how filament properties are affected by the selection of parameters in the DisPerSE algorithm. They determined that raising the persistence threshold can remove a substantial portion of short filaments and that the skeleton-smoothing process does not significantly alter the filament length distributions.

In simulation, based on filaments traced by DisPerSE from the large hydrodynamic Illustris-TNG simulation, Galárraga-Espinosa et al. (2020) investigated the population of filament lengths and radial density profiles. They claimed that short and long filaments do not have the same radial density profiles. For the total population of filaments from the MillenniumTNG simulations, Galárraga-Espinosa et al. (2024) found very little evolution of the filament length distributions or radial density profiles. Using filaments connecting group-mass halo pairs in a dark matter only simulation, Yang et al. (2022) provided a universal function with four parameters to fit the filament radial density profiles. They found that the scale radii parameters have little evolution with redshift but increase with filament length, indicating that filaments of different lengths actually follow different evolution histories.

However, the statistical properties of filaments depend not only on the identification algorithms but also on the different tracers, such as dark-matter particles or galaxies. Unlike relatively spherical haloes, filaments are more complex because of their elongated shape. The measurement of filament lengths is influenced by the way their endpoints are determined, a process often impacted by the settings used in their identification methods (Bond et al. 2010; Malavasi et al. 2020). Rost et al. (2020) compared three SDSS filament catalogues identified by different identification techniques (Tempel et al. 2014; Martínez et al. 2016; Pereyra et al. 2020). It was observed that the characteristics of filaments vary significantly with the choice of identification methods. Using the DisPerSE algorithm on the semi-analytical model's results, Zakharova et al. (2023) explored the attributes of filaments derived from both model galaxies and dark-matter particles. The investigation revealed that filaments associated with dark-matter particles consistently exhibit greater lengths compared to those derived from galaxies. The process of extracting filaments was asserted to be heavily dependent on the tracers used and the settings implemented in the DisPerSE algorithm.

The statistical characteristics of filaments, as observed and simulated, are still not well understood. This study examines these charac-

teristics through the use of the COWS algorithm (Pfeifer et al. 2022) and the ELUCID simulation (Wang et al. 2014, 2016, 2018), which are constrained by the density field of the galaxy distribution, thereby connecting the simulated dark matter distribution with the actual observations of the galaxy distributions (Zhang et al. 2021a,b, 2022b), with a specific focus on offering a quantitative analysis of the statistical properties of filaments. The COWS method applies a medial axis thinning algorithm (Zhang & Suen 1984; Lee et al. 1994) to the cosmic web's velocity shear tensor (V-web) to identify the filament skeleton, maintaining topological and geometric constraints. In this study, we use the Hessian matrix of the density field to classify the cosmic web environment instead of using the velocity shear tensor data set used in Pfeifer et al. (2022). Additionally, the connection between the ELUCID simulation and SDSS observations (Yang et al. 2018) allows further investigation into differences in filament extraction and analysis across both dark-matter and galaxy distributions in future studies.

The structure of this paper is organised as follows. In Section 2, we provide an overview of the ELUCID N body simulation, the cosmic web classification algorithm based on the smoothed density field, and the COWS filament finding method. In Section 3, we present a statistical study of the filamentary structures of the cosmic web, such as the filament length distribution and the radial density profile. Finally, we summarise our results in Section 4.

2 DATA AND METHOD

The data used in this paper are from the constrained ELUCID simulation (Wang et al. 2014, 2016, 2018), which can reproduce the density field of the nearby universe generated from the galaxy group distributions in the SDSS observation (Yang et al. 2007, 2012). As expected, the statistical properties of cosmic filaments are well reproduced in the ELUCID simulation compared to the SDSS observation (Wang et al. 2016).

The ELUCID simulation is a dark matter only cosmological simulation with 3072^3 particles evolved in a periodic box of $500 h^{-1} \text{Mpc}$ on a side from an initial redshift of $z = 100$ to the present. The initial condition of the ELUCID simulation is constrained by the density field of the galaxy distribution of Sloan Digital Sky Survey Data Release 7 (SDSS DR7; Abazajian et al. 2009), employing the Hamiltonian Markov Chain Monte Carlo (HMC) algorithm combined with Particle Mesh (PM) dynamics (Wang et al. 2014). The initial density field evolved to the present day using L-Gadget, a memory-optimised version of Gadget-2 (Springel 2005), with 100 snapshot output from $z = 18.4$ to $z = 0$. In this work, we only use the distribution of dark matter particles at redshift $z = 0$. The mass of each dark-matter particle is $3.1 \times 10^8 h^{-1} \text{M}_\odot$. The adopted cosmological parameters are $\Omega_m = 0.258$, $\Omega_b = 0.044$, $\Omega_\Lambda = 0.742$, $h = 0.72$, $n_s = 0.963$, and $\sigma_8 = 0.796$.

In the simulation, the standard Friends-of-Friends (FOF) method is applied to the particle data to generate FOF haloes, using a linking length of $b = 0.2$ times the average particle separation. Subsequently, the SUBFIND algorithm splits each FOF halo into individual subhaloes by applying a gravitational binding procedure during the unbinding phase. The total count of subhaloes in the ELUCID simulation is 48, 846, 170 with masses exceeding $10^{9.8} h^{-1} \text{M}_\odot$.

The observational data used in this research comes from SDSS (Abazajian et al. 2009), known as one of the most important astronomical surveys. Utilizing multi-band imaging and spectroscopic data from SDSS DR7, Blanton et al. (2005) created the New York University Value-Added Galaxy Catalogue (NYU-VAGC) incorpo-

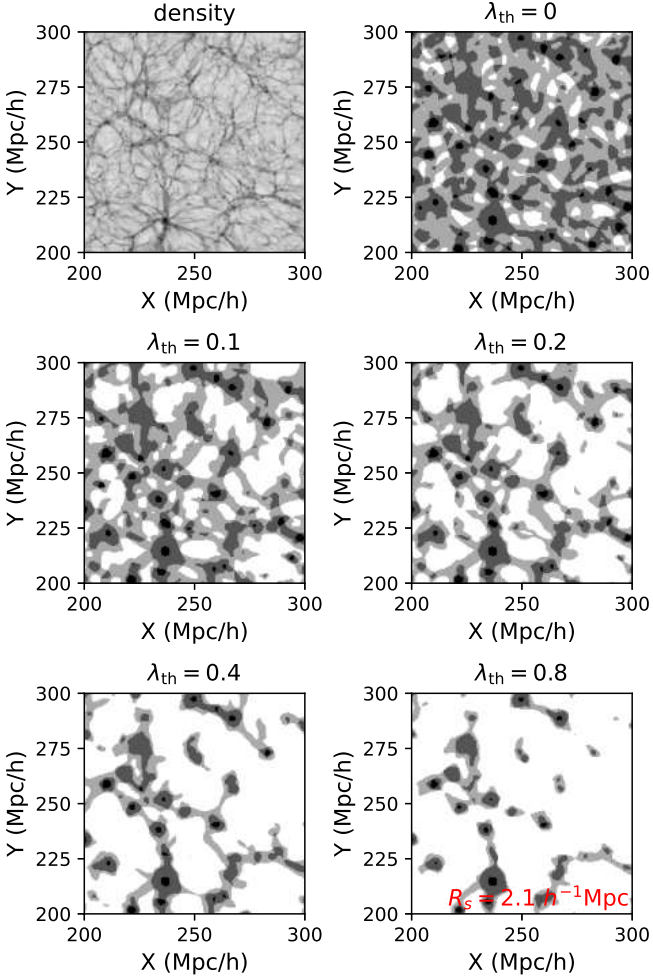


Figure 1. Density distribution and the cosmic web classifications in a slice of width $0.5 h^{-1} \text{Mpc}$. The upper-left panel shows the projected logarithmic density distribution, where darker areas indicate higher density. The other panels show the environment classifications with the smoothing length $R_s = 2.1 h^{-1} \text{Mpc}$ in different values of the thresholds $\lambda_{\text{th}} = 0, 0.1, 0.2, 0.4, 0.8$, according to which the grid cells are classified into knots (black), filaments (dark grey), sheets (light grey), and voids (white), respectively.

rating a unique set of enhanced reductions. From the NYU-VAGC, we gathered a total of 639,359 galaxies with redshifts in the interval $0.01 \leq z \leq 0.2$, redshift completeness $C_z > 0.7$, and extinction-corrected apparent magnitudes brighter than $r \leq 17.72$. The coverage area of 639,359 galaxies spans 7,748 square degrees, divided into two sections: an extensive continuous area in the Northern Galactic Cap and a smaller section in the Southern Galactic Cap. The galaxy distribution in SDSS DR7 is linked to the dark matter structure pinpointed by the constrained ELUCID simulation (Yang et al. 2018).

2.1 Cosmic web classification algorithm

The cosmic web type at any point in space can be classified by the Hessian matrix of the density field (hereafter D-web), which was pioneered by Colombi et al. (2000). The Hessian matrix, adjusted by a negative normalization, of the smoothed density field is specified

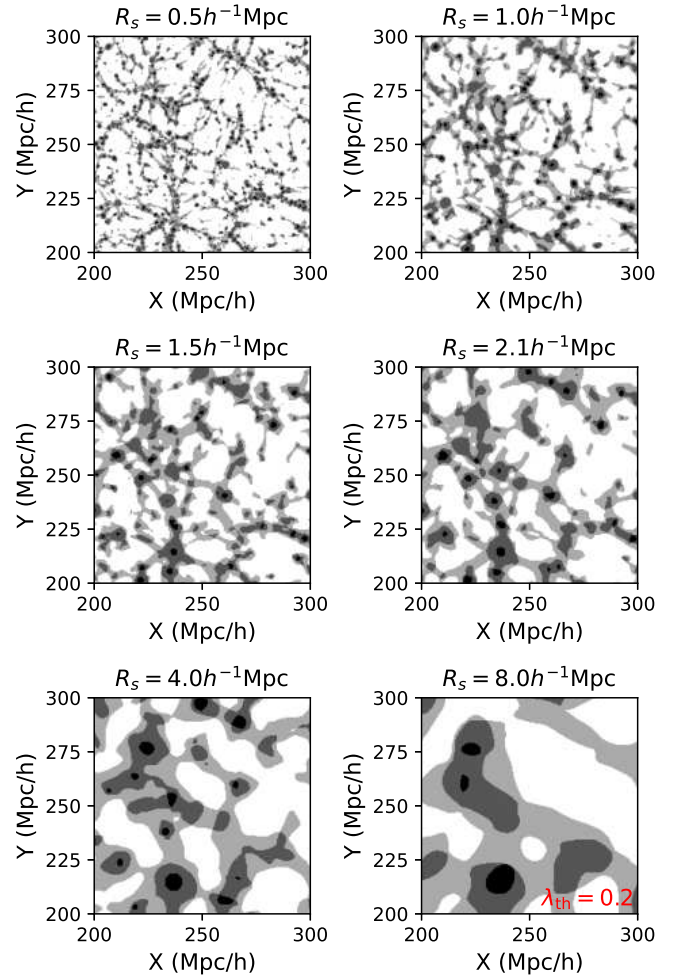


Figure 2. Similar to Figure 1 but for different Gaussian smoothing lengths $R_s = 0.5, 1.0, 1.5, 2.1, 4.0, 8.0 h^{-1} \text{Mpc}$ at fixed threshold $\lambda_{\text{th}} = 0.2$.

for each grid cell as follows:

$$H_{ij} = -\frac{R_s^2}{\rho_{\text{mean}}} \frac{\partial^2 \rho_s}{\partial x_i \partial x_j}, \quad (1)$$

where ρ_s represents the smoothed density field employing a Gaussian filter with a smoothing length R_s , and ρ_{mean} denotes the universal average matter density. A negative sign is incorporated on the right-hand side of Equation 1 to ensure that positive (negative) eigenvalues indicate collapsing (expanding) matter, aligned with the eigenvalue signs of the tidal tensor in the dynamic model (Hahn et al. 2007). The classification of environments is determined by the count of eigenvalues that exceed a specified threshold λ_{th} . Specifically, the counts of 0, 1, 2, or 3 are indicative of voids, sheets, filaments, and knots, in the order (Forero-Romero et al. 2009).

To calculate the Hessian matrix of the density field H_{ij} , Cloud-in-Cell (CIC) interpolation of 1024^3 cells is used to construct the density field ρ_{cic} for 3072^3 particles in a periodic box of $500 h^{-1} \text{Mpc}$, resulting in an average of 27 particles in each cell to ensure that few if any cells are empty. The CIC density field ρ_{cic} is then smoothed with a Gaussian kernel with width R_s to generate the smoothed density ρ_s , to calculate the eigenvalues of the Hessian symmetric matrix in Equation 1 at the position of each cell. Following convention, eigen-

values are denoted by λ_1, λ_2 and λ_3 ($\lambda_1 > \lambda_2 > \lambda_3$), corresponding to the eigenvectors \hat{e}_1, \hat{e}_2 and \hat{e}_3 . The cosmic web type for each cell is classified by counting the number of eigenvalues with $\lambda_i > \lambda_{th}$, where $i = 1, 2$, or 3 . Note that the environment classification is local for each cell, and the collection of neighboring cells with the same cosmic web type defines the geometrical constructions named voids, sheets, filaments, or knots. For filament cells, the eigenvectors \hat{e}_3 can be used to indicate the directions of the filaments (Zhang et al. 2009, 2013, 2015).

Obviously, the D-web method depends on two free parameters R_s and λ_{th} , which are typically chosen such that the environment classification reproduces the visual impression of the cosmic web. Figure 1 shows the density distribution and the classifications of the cosmic web at fixed smoothing length $R_s = 2.1 h^{-1} \text{Mpc}$ for different thresholds $\lambda_{th} = 0, 0.1, 0.2, 0.4$, and 0.8 , where the grid cells are classified into knots (black), filaments (dark grey), sheets (light grey) and voids (white), respectively. As shown in Figure 1, for $\lambda_{th} = 0$, the volume filling fraction of the voids is very small, which contrasts with the visual impression of the voids in the density distribution. Obviously, the volume fraction of the voids increases with the threshold. For $\lambda_{th} \geq 0.1$, the voids occupy a large fraction of the simulated volume, which appears to reproduce the visual impression of the cosmic web in the simulation.

For cells in a grid, the classifications of the cosmic web depend not only on the threshold parameter λ_{th} , but also on the smoothing length R_s . Figure 2 shows the cosmic web classifications for different smoothing lengths $R_s = 0.5, 1.0, 1.5, 2.1, 4.0, 8.0 h^{-1} \text{Mpc}$ at a fixed threshold $\lambda_{th} = 0.2$. Figure 2 shows that increasing the smoothing lengths eliminates a large fraction of less significant filaments. The smoothing procedure can remove sharp directional changes and nonphysical edges in filaments due to the noise of the density distribution. In this study, the cell size of the grid is approximately $0.5 h^{-1} \text{Mpc}$. Using larger smoothing lengths can alleviate the effect of shot noise on the filament geometry. In the following analysis, we focus mainly on the cosmic web classifications identified with the smoothing length $R_s \geq 1 h^{-1} \text{Mpc}$ and the threshold parameters $\lambda_{th} \geq 0.1$.

2.2 Filament finding algorithm: COWS

In this work, the filament axes are identified by a medial axis thinning algorithm (Lee et al. 1994) applied in the COWS method¹ (Pfeifer et al. 2022).

Figure 3 presents a depiction of the COWS technique to identify filament spines within the ELUCID simulation. The upper left panel of Figure 3 displays the input data in which the cosmic web classifications are determined using the Hessian matrix of the density field, as described in Section 2.1, rather than employing the velocity shear tensor mentioned in Pfeifer et al. (2022). As shown in the upper right panel of Figure 3, the cosmic web classifications are then transformed into binary data with a value of 1 (black region) for knot and filament cells and a value of 0 (white region) for sheets and void cells. Next, the medial axis thinning algorithm (Lee et al. 1994) is used to reduce large amounts of binary data to representations that span one cell by identifying and removing border cells while preserving the geometric and topological features of the data. The lower left panel of Figure 3 shows the medial axes of the set of cells within the black region of the upper right panel. The medial axes are often called the topological skeleton, which has the same connectivity as

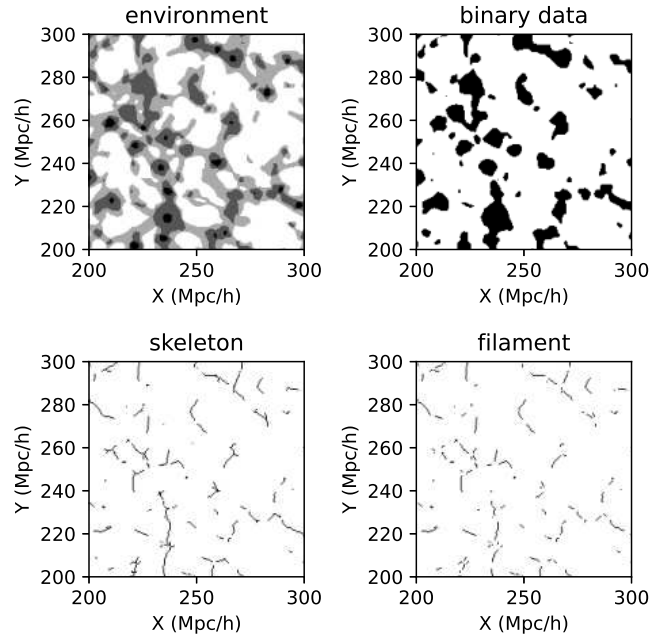


Figure 3. Illustration of the COWS method to find the filament spine based on the cosmic web classifications identified by the D-web method. Upper-left: Cosmic web environment identified by the Hessian matrix of the density field. Upper-right: Binary data with a value of 1 (black region) identified as knots and filaments, and a value of 0 (white region) identified as sheets and voids. Lower-left: Skeleton classification using the medial axis thinning method. Lower-right: Filaments identified by removing cavities (blobs) and junctions in the skeleton.

the original data. Finally, individual filaments are defined by removing any unwanted contaminants or features, such as junctions and hollow cavities, from the topological skeleton.

Figure 4 illustrates the distribution of dark matter density and filaments across a $10 h^{-1} \text{Mpc}$ slice of the ELUCID simulation, highlighting areas of greater density with darker shades. Generally, the resulting filaments in red trace the majority of visible filamentary structures very well in Figure 4.

The axis thinning algorithm to identify filaments from the D-web has no free parameter. However, the D-web method itself has two parameters, the smoothing length R_s and the threshold λ_{th} , which can affect the filament catalogue extracted from the density distribution of dark matter particles. It is interesting to investigate the dependence of the statistical properties of filaments on the free parameters. For the case of $R_s = 2.1 h^{-1} \text{Mpc}$ and $\lambda_{th} = 0.2$, the identified filaments are coloured red as shown in Figure 4. Note that each filament identified by COWS has two end points connected by a single path with one cell width, which can be used to calculate the filament length and the density profile perpendicular to the filament axis.

3 RESULTS

Using the filament catalogue identified by the COWS method from the ELUCID simulation, we focus mainly on the statistical properties of filaments, such as the filament length distributions and the density profiles.

¹ <https://github.com/SimonPfeifer/cows>

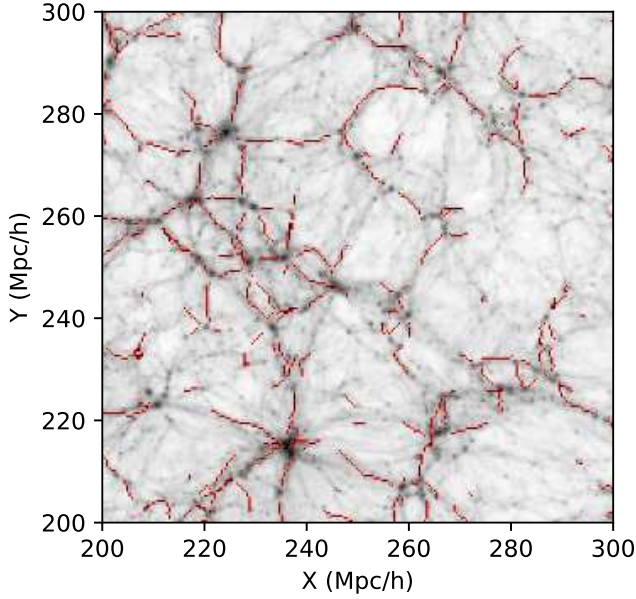


Figure 4. Density and filament distribution in a slice of width $10 h^{-1} \text{Mpc}$ from the ELUCID simulation. The filament spine in red is identified by the COWS method, based on the cosmic web classifications with $R_s = 2.1 h^{-1} \text{Mpc}$ and $\lambda_{\text{th}} = 0.2$.

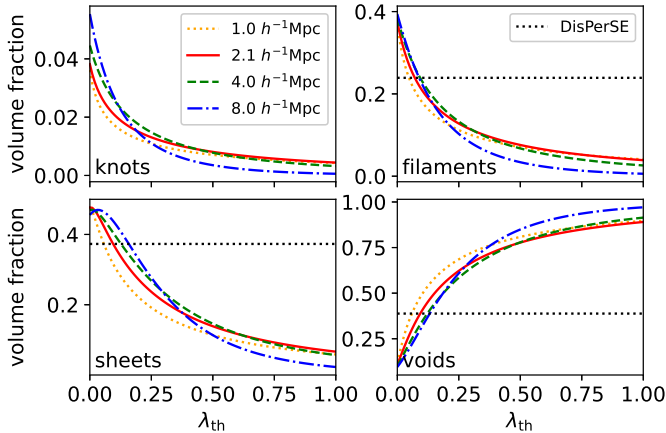


Figure 5. Volume fractions of knots, filaments, sheets and voids as a function of the threshold λ_{th} with different smoothing lengths $R_s = 1.0, 2.1, 4.0, 8.0 h^{-1} \text{Mpc}$. For comparison, the black dotted line represents the volume fractions derived using the DisPerSE method, as detailed in Table 2 of Libeskind et al. (2018).

3.1 Volume fraction

Based on the cosmic web classification using the D-web method, we investigate the dependence of the volume fractions for different types of cosmic webs on the free parameters R_s and λ_{th} . For a more detailed comparison of different methods, we refer the reader to Table 2 and Figure 5 in Libeskind et al. (2018).

Volume fractions are measured for knots, filaments, sheets, and voids by varying the threshold λ_{th} from 0 to 1 at fixed smoothing

lengths $R_s = 1.0, 2.1, 4.0, 8.0 h^{-1} \text{Mpc}$, as shown in Figure 5. Generally, the volume fraction for each type of cosmic web is strongly dependent on the threshold parameter λ_{th} . For knots, filaments, and sheets, the volume fractions decrease with increasing threshold λ_{th} , while the volume fraction of the voids increases with increasing λ_{th} . At fixed $R_s = 2.1 h^{-1} \text{Mpc}$ represented by the solid red lines in Figure 5, the volume filling fraction of the filaments decreases from 37.5% to 3.9% for increasing λ_{th} from 0 to 1, while the volume fraction of the voids increases from 11.0% to 89.0% for λ_{th} between 0 and 1.

Additionally, the volume fraction of each environment is weakly dependent on the smoothing length. For the case of $\lambda_{\text{th}} = 0$, there is almost no dependence on the smoothing length R_s for the volume fractions of filaments, sheets, and voids. For the case of $\lambda_{\text{th}} \geq 0.4$, the volume fraction of the filaments decreases with increasing smoothing length, contrary to the trend of $\lambda_{\text{th}} \lesssim 0.1$ where larger smoothing lengths correspond to larger volume fractions, as shown in the upper right panel of Figure 5.

3.2 Filament orientation

In this study, the filament axis is a single path with a cell width, indicating the medial axis of the filament cells identified by the D-web method. The filament axis in the COWS method is expected to be aligned with the eigenvector \hat{e}_3 of the Hessian density matrix in equation 1. In the following analysis, we investigate the directions of the filaments in the COWS method with respect to the eigenvector \hat{e}_3 in the D-web method.

In the COWS approach, a filament consists of two terminal points linked by a continuous chain of connected cells. Following Pfeifer et al. (2022), the direction \mathbf{d}_i of the filament cell i is calculated by its two neighbours named $i+1$ and $i-1$,

$$\mathbf{d}_i = \mathbf{p}_{i+1} - \mathbf{p}_{i-1}, \quad (2)$$

where \mathbf{p}_{i+1} and \mathbf{p}_{i-1} are the positions of the two neighbour cells $i+1$ and $i-1$. For the terminal point in a filament, the direction \mathbf{d}_i is set to be the vector between the end point and its neighbour.

In the D-web method, the eigenvalues of the density Hessian matrix are calculated to quantify the collapsed or expanding matter. The corresponding eigenvectors indicate the local orientation of the morphological structure. The filament cells in the D-web method are identified where the eigenvalues are $\lambda_1 > \lambda_{\text{th}}$, $\lambda_2 > \lambda_{\text{th}}$, and $\lambda_3 < \lambda_{\text{th}}$. The eigenvector \hat{e}_3 of the density Hessian matrix can be used to indicate the direction of the filament in the D-web. To verify the validity of filament finding methods, we calculate the alignment between the direction of the filament \mathbf{d}_i and \hat{e}_3 .

According to the definition of the filament direction given in Equation 2, for a filament cell with two neighboring cells, the connection between these two neighbors should be considered as an axis rather than a vector, because the order in which the neighbors are chosen does not matter. Therefore, the alignment is assessed by calculating the absolute value of the dot product between the filament direction and \hat{e}_3 . Figure 6 shows the probability distribution function (PDF) of the absolute cosine of the angle θ between the direction of the filament \mathbf{d}_i in COWS and the eigenvector \hat{e}_3 in D-web, where $\cos \theta = \mathbf{d}_i \cdot \hat{e}_3 / |\mathbf{d}_i|$. In the absence of any alignment, the probability distribution is flat with a constant value of 1. The average values of $|\cos \theta|$ are also shown in the panels of Figure 6. The values of $\langle |\cos \theta| \rangle = 1$ imply that the direction of the filament \mathbf{d}_i in COWS is parallel to the eigenvector \hat{e}_3 in the D-web, while the values of $\langle |\cos \theta| \rangle = 0$ indicate perpendicular orientations.

The left panel of Figure 6 shows the PDF for different smoothing

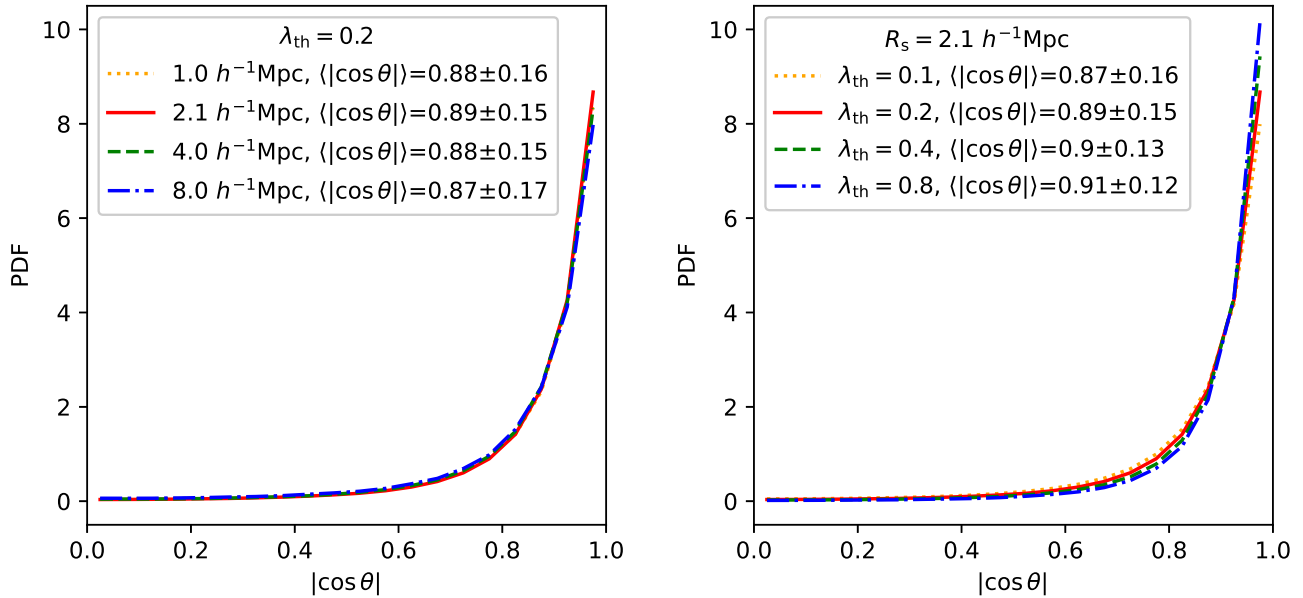


Figure 6. Probability distribution function (PDF) of the cosine of the angle θ between the filament direction in COWS and the eigenvector \hat{e}_3 in D-web. The left panel shows the PDF for different R_s at fixed threshold $\lambda_{\text{th}} = 0.2$, while the right panel shows the PDF for different thresholds λ_{th} at fixed $R_s = 2.1 h^{-1} \text{Mpc}$. The mean values of $|\cos \theta|$ and the standard errors are indicated in the panels.

scales R_s with mean values and standard errors of $|\cos \theta|$. The filament orientations for each smoothing scale R_s are compared to the corresponding eigenvectors \hat{e}_3 for those values of R_s . The alignment signals for different values of R_s are nearly the same and remain largely unchanged with variations in smoothing lengths. The left panel of Figure 6 illustrates that the orientations of the filaments are primarily aligned with the eigenvector \hat{e}_3 in the D-web, validating the efficiency of the axis thinning algorithm in detecting the filament axis.

The right panel of Figure 6 shows the PDF for different thresholds λ_{th} at fixed $R_s = 2.1 h^{-1} \text{Mpc}$. The alignment signals become slightly stronger for increasing thresholds, with $\langle |\cos \theta| \rangle = 0.91 \pm 0.15$ for $\lambda_{\text{th}} = 0.8$. Obviously, the filament spines are strongly aligned with the eigenvector \hat{e}_3 characterised by the underlying density field, indicating the validity of the COWS methods.

3.3 Filament length distribution

In this section, we explore the distribution of lengths for filaments traced by dark matter particles in the ELUCID simulation. The length of the filament L is defined as the distance along the filament path, which is delineated by the medial axis of the filament cells identified using the D-web method. To calculate the length of each filament, we sum the distances between the midpoints of adjacent cells and include an additional cell size to account for the two half-ends of the filament (Pfeifer et al. 2022).

An isolated spherical over-density should not be classified as a real filament, but the filament finder would identify an isolated spherical over-dense structure as a filament of length on the order of the smoothing scale (Bond et al. 2010; Choi et al. 2010). Based on the filament catalogue, we have calculated the number distribution of filament lengths for different smoothing scales R_s . We find that the number distribution of filament lengths exhibits a dramatic drop-off below the smoothing length, in agreement with the results of

Bond et al. (2010). Therefore, we hereafter exclude non-physical filaments whose lengths are shorter than the smoothing length R_s . We focus only on filaments of length $L \geq R_s$, resulting in a total number of filaments $N_f = 979\,552, 178\,417, 35\,353$ and $5\,248$ for $R_s = 1.0, 2.1, 4.0,$ and 8.0 , respectively. Obviously, the total number of filaments decreases dramatically with increasing smoothing scales R_s .

The halo-mass distribution is conventionally described by halo mass function. In spirit of the halo mass function, the filament length function (LF) can be defined as the number density of filaments per logarithmic unit of length. For comparison, we also calculate the probability distribution function (PDF) $f(L)$ of filament lengths. Figure 7 shows the filament LFs and PDFs for varying the smoothing length R_s (top) and the threshold λ_{th} (bottom) in the simulation of $500 h^{-1} \text{Mpc}$ on one side.

The upper left panel of Figure 7 shows the filament LF for different smoothing scales $R_s = 1.0, 2.1, 4.0$ and $8.0 h^{-1} \text{Mpc}$ at a fixed threshold $\lambda_{\text{th}} = 0.2$. Generally, the median lengths of the filament increase with the smoothing scales R_s , which is evident in the ranges covered by different filament length functions. Moreover, our observations indicate that LF typically reaches a maximum at $L \approx 2.5 R_s$, for example, from approximately $5.3 h^{-1} \text{Mpc}$ at $R_s = 2.1 h^{-1} \text{Mpc}$ to approximately $20.0 h^{-1} \text{Mpc}$ at $R_s = 8.0 h^{-1} \text{Mpc}$. Furthermore, the number of short filaments decreases with increasing smoothing scales, while the number of long filaments increases with larger R_s .

The upper right panel of Figure 7 shows the probability distribution function of the filament lengths. Obviously, short filaments dominate the catalogue of $R_s = 1.0 h^{-1} \text{Mpc}$, while long filaments are easily detected in the case of $R_s = 8.0 h^{-1} \text{Mpc}$. Interestingly, we find that the logarithmic PDFs of different smoothing scales are approximately proportional to the filament lengths expressed by $\log f(L) \propto L$, where $f(L)$ is the PDF.

Next, we investigate the dependence of the filament LF and PDF on the threshold parameter λ_{th} . The lower panels of Figure 7 show

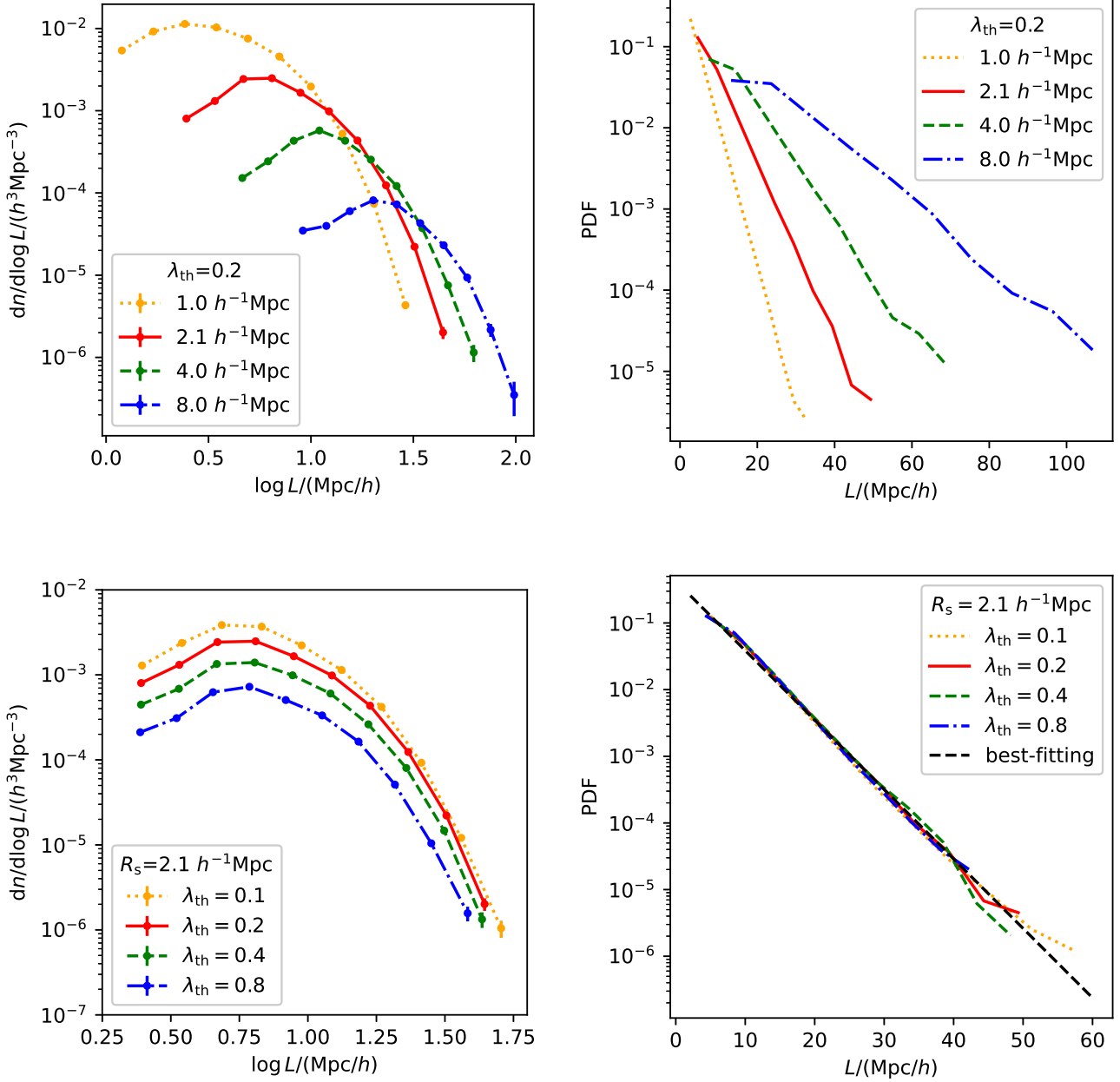


Figure 7. Length distributions of filaments for varying the smoothing length R_s (upper panels) and the threshold λ_{th} (lower panels) in the simulation of $500 h^{-1}\text{Mpc}$ on a side. The filament length function is shown in the left panels with Poisson errors included. The right panel shows the probability distribution function of the filament lengths. In the lower right panel, the black dashed line represents the best-fitting relation of the form $\log f(L) = -0.1L - 0.37$, where $f(L)$ is the probability density function.

the filament LF and PDF for different thresholds $\lambda_{\text{th}} = 0.1, 0.2, 0.4$, and 0.8 at fixed $R_s = 2.1 h^{-1}\text{Mpc}$. In the entire range, the filament length functions decrease with increasing thresholds from 0.1 to 0.8 , as shown in the lower left panel of Figure 7. In the D-web method, the adoption of larger thresholds can lead to a decrease in the number of short and long filaments throughout the range. For $R_s = 2.1 h^{-1}\text{Mpc}$, the total number of filaments $N_f = 274\,842, 178\,417, 100\,626$ and $48\,719$ for $\lambda_{\text{th}} = 0.1, 0.2, 0.4$ and 0.8 , respectively.

In the lower right panel of Figure 7, the PDFs of different thresholds are consistent with each other, indicating that the probability of

filament lengths does not change with the variation of threshold parameters. PDF $f(L)$ with fixed smoothing length $R_s = 2.1 h^{-1}\text{Mpc}$ can be expressed by the best fit relation $\log f(L) = -0.1L - 0.37$, shown by the black dashed line in the lower right panel of Figure 7.

3.4 Filament density profile

In this section, we investigate the density distribution of filaments identified by dark-matter particles in the ELUCID simulation. For

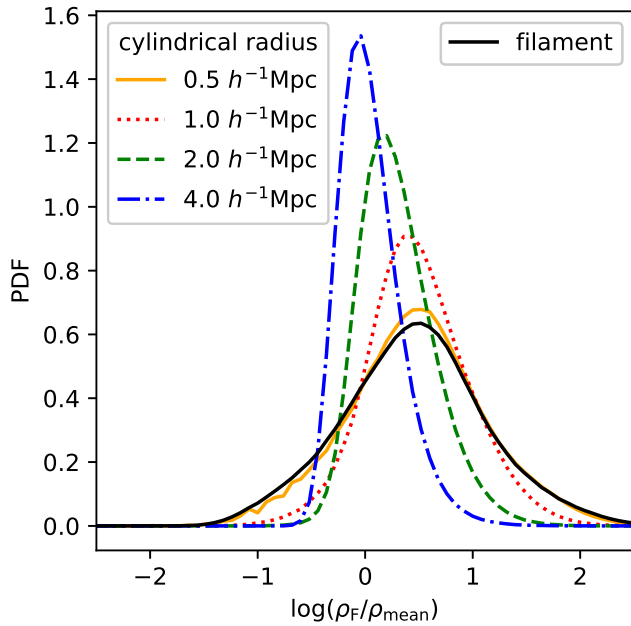


Figure 8. Probability distribution function (PDF) of the logarithmic density contrast of the filament segments for varying the cylindrical radii. For a segment in a filament, the segment density is calculated by counting the number of dark matter particles in the cylindrical segment with the radius of $r = 0.5$ (orange), 1.0 (red), 2.0 (green), or $4.0 h^{-1}\text{Mpc}$ (blue). For reference, the black solid line illustrates the probability distribution function of the densities of filament cells determined by the COWS method.

each segment in a filament, the density of the segment is defined as

$$\rho_{\text{F}}(\leq r) = \frac{m_{\text{p}} N_{\text{p}}}{\pi r^2 l}, \quad (3)$$

where m_{p} is the particle mass, N_{p} is the number of dark matter particles in the cylindrical segment, r is the radial distance to the axis of the segment, and l represents the length of the segment, calculated as the distance between adjacent filament cells, expressed as $l = |\mathbf{p}_{i+1} - \mathbf{p}_i|$, where \mathbf{p}_{i+1} and \mathbf{p}_i are the positions of these neighbouring filament cells. According to Equation 3, the mass density of the filament can be calculated by counting the number of particles in the cylindrical segment within the radius of r .

Figure 8 shows the probability distribution function of the logarithmic density contrast of the filament segments for varying the cylindrical radii at $r = 0.5, 1.0, 2.0,$ or $4.0 h^{-1}\text{Mpc}$, respectively. The COWS filament is made up of a single pathway of connected cells, which is a subset of cells classified as filaments in the density Hessian matrix method. For reference, the solid black line in Figure 8 depicts the density distribution of the filament cell determined by the COWS method. In particular, the filament cell density distribution (black) is very similar to the PDF for $r = 0.5 h^{-1}\text{Mpc}$ (orange), considering that the cell size in this investigation is around $0.5 h^{-1}\text{Mpc}$. Clearly, the filament density is significantly influenced by the radius chosen for the cylindrical filament. Smaller radii result in higher filament densities and wider density distributions. The density of filament segments would rapidly approach the cosmic mean density (ρ_{mean}) along with the increase of the cylindrical radius, leading to narrower distributions.

We subsequently evaluated the radial density profile of the filaments, which represents the density distribution along the orthogo-

nal direction to the filament axis. A filament is composed of several interconnected segments. In practice, the radial density is assessed by investigating the dark-matter density distribution surrounding individual segments within the filaments. Each cylindrical segment i is partitioned into cylindrical shells 40 using uniform logarithmic bins centred on its axis, spanning from the core of the segment to $r = 20 h^{-1}\text{Mpc}$. The distribution of particles within each radial shell determines its density. Specifically, the density of the j -th shell of the segment i is calculated as

$$\rho_{ij} = \frac{m_{\text{p}} N_{ij}}{\pi(r_{j+1}^2 - r_j^2)l_i} \quad (4)$$

where the index j denotes the j -th cylindrical shell with thickness $r_{j+1} - r_j$, l_i is the length of segment i , and N_{ij} is the particle count within the j -th shell of segment i . The average density ρ_j for the j -th cylindrical shell is determined by computing the mean of the density profiles from all segments, as given by

$$\rho_j = \frac{1}{N_s} \sum_{i=1}^{N_s} \rho_{ij}, \quad (5)$$

where N_s represents the total number of segments.

Figure 9 shows the density profile of the filaments as a function of the radial distance r from the filament axes. The density ρ has been normalised by the mean density ρ_{mean} of the universe. The error bars depicted in Figure 9 are derived by bootstrapping the segment profiles utilising the method `astropy.stats.bootstrap` from the `Astropy` package². From the entire set of N_t segments, a subset is chosen at random and their mean values are determined. This random selection and computation of averages is repeated 100 times, resulting in 100 different mean values. The standard error, derived from these 100 mean values, corresponds to the error bars presented in Figure 9.

The left panel of Figure 9 shows the radial density profile of the filaments for different smoothing lengths $R_s = 1.0, 2.1, 4.0$ and $8.0 h^{-1}\text{Mpc}$ at a fixed threshold $\lambda_{\text{th}} = 0.2$. Obviously, the density profile of the filaments depends on the smoothing scale R_s . In general, the density profile shown in Figure 9 agrees with the results of similar previous studies (Galárraga-Espinosa et al. 2020; Pfeifer et al. 2022; Galárraga-Espinosa et al. 2024). The density profile of filaments exhibits an excess with respect to the mean density of the Universe. For different smoothing lengths R_s , the density profile decreases with increasing radial distance r , until it reaches a valley approximately twice the smoothing length, i.e., about $2R_s$. It should be noted that the density profile that shows a valley and a minor peak in the outer regions of the filaments was also reported in previous studies by Pfeifer et al. (2022) and Yang et al. (2022). In contrast, in studies by Galárraga-Espinosa et al. (2020) and Galárraga-Espinosa et al. (2024), these characteristics are less pronounced. The valley in the radial density profile might stem from the technique used to generate the density field using CIC interpolation in the COWS method. The COWS method depends on various types of cosmic web cells classified on a uniform grid, whereas DisPerSE detects filaments by analysing the topological features of the density field. This field can be obtained using either the Delaunay Tessellation Field Estimator (DTFE) or the CIC approach, based on the spatial distribution of the input particles. Using data from the MillenniumTNG simulation (Hernández-Aguayo et al. 2023), we investigated the density profiles around filaments recognised by DisPerSE using both CIC and DTFE

² <http://www.astropy.org>

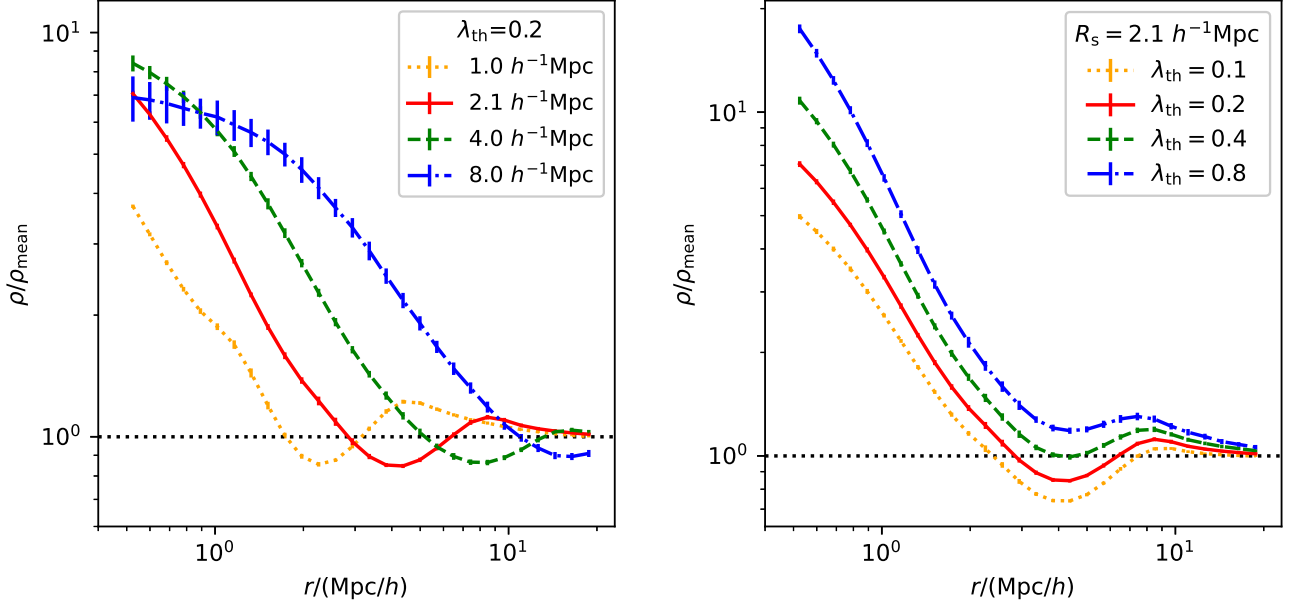


Figure 9. Density profile of filaments as a function of the radial distance r to the filament axes. The left panel shows the radial density profile of filaments detected by different values of smoothing lengths at a fixed threshold $\lambda_{\text{th}} = 0.2$, while the right panel shows the density profile of filaments for different thresholds at a fixed smoothing length $R_s = 2.1 h^{-1} \text{Mpc}$. The error bars are measured from 100 bootstrap samples.

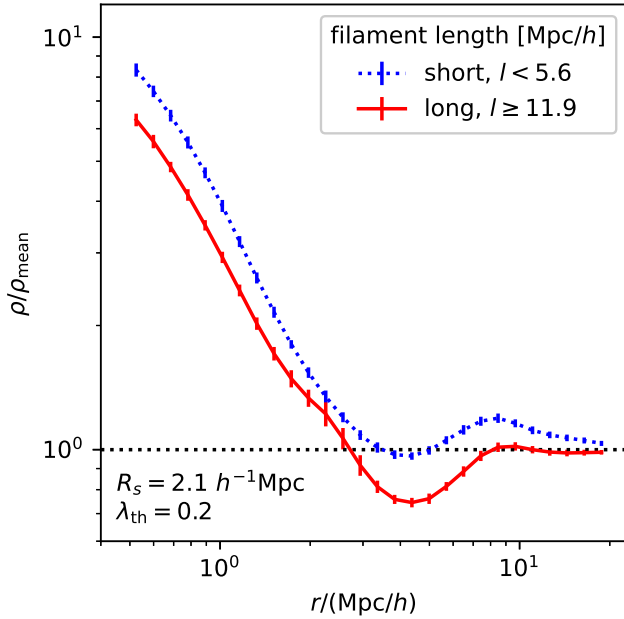


Figure 10. Radial density profile of short (blue) and long (red) filaments based on the environment classification of $R_s = 2.1 h^{-1} \text{Mpc}$ and $\lambda_{\text{th}} = 0.2$.

density constructions. We found that employing the CIC method in DisPerSE for generating density leads to a valley feature in the density profile, whereas this feature is absent when the DTFE method is used for density construction (Galárraga-Espinosa et al. 2024; Wang et al. 2024a).

The right side of Figure 9 illustrates the density profiles of fila-

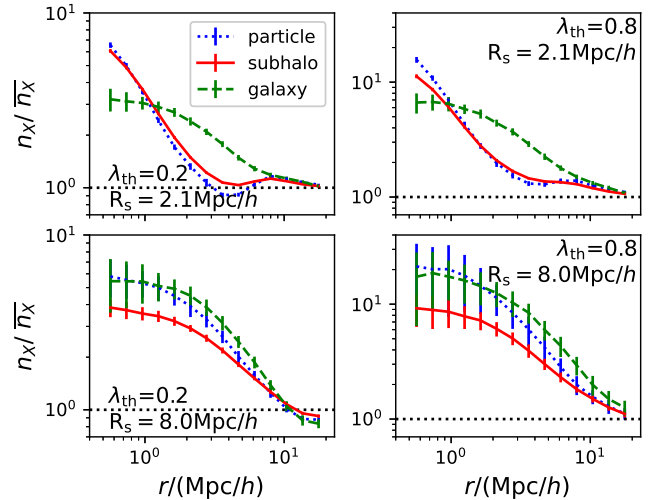


Figure 11. Number density profiles of dark matter particles (blue), subhaloes (red), and galaxies (green) around filaments. The various panels display results for filaments categorised by different parameters R_s and λ_{th} .

ments at varying thresholds $\lambda_{\text{th}} = 0.1, 0.2, 0.4$ and 0.8 with a constant smoothing length $R_s = 2.1 h^{-1} \text{Mpc}$. Clearly, as the thresholds increase, so do the amplitudes of the density profiles, suggesting that larger thresholds capture filaments of higher density and greater significance. This observation aligns with Figure 1, where higher thresholds effectively exclude less dense, indistinct filaments.

Recently, Galárraga-Espinosa et al. (2020) claimed that short and long filaments have different statistical properties. In this study, we investigate the density profiles of short and long filaments for the catalogue of $R_s = 2.1 h^{-1} \text{Mpc}$ and $\lambda_{\text{th}} = 0.2$. We divide the fila-

ment catalogue into four different samples so that each contains the same number of segments and the separation points are 5.6, 8.0, and $11.9 h^{-1}\text{Mpc}$. Figure 10 shows the radial density profiles of the short ($L < 5.6 h^{-1}\text{Mpc}$) and long ($L > 11.9 h^{-1}\text{Mpc}$) filaments for the cases of $R_s = 2.1 h^{-1}\text{Mpc}$ and $\lambda_{\text{th}} = 0.2$. We can see that the short and long filaments have significantly different radial density profiles. Short filaments have higher density profiles than long filaments at all radial distances, which is in agreement with the filament density profiles by the DisPerSE method in Galárraga-Espinosa et al. (2020).

Next, we examine the number density profiles surrounding filaments for galaxies as well as subhaloes. The spatial distribution of galaxies in SDSS DR7 is associated with the dark-matter distribution in the constrained ELUCID simulation. This linkage is due to the simulation's use of initial conditions constrained by the mass density field obtained from the SDSS DR7 galaxy distribution.

To ascertain the number density profiles of galaxies, the spatial coordinates (ra, dec, z) of galaxies recorded by SDSS are converted into the (X, Y, Z) coordinate system employed in the ELUCID simulation. Subsequently, we measured the number density of galaxies, subhaloes, and particles around the filament axes identified in the ELUCID simulation. To ensure a fair comparison, we excluded particles and subhaloes in the ELUCID simulation that fall outside the survey sky coverage area. Figure 11 illustrates the number density profiles $n_X/\overline{n_X}$ from the filament axes, where n_X is the number density at the radial distance r from the filament axes, X represents galaxies, subhaloes or particles, and $\overline{n_X}$ signifies their mean value. The different panels in Figure 11 present data for filaments classified by parameters $R_s = 2.1, 8.0 h^{-1}\text{Mpc}$ and $\lambda_{\text{th}} = 0.2, 0.8$. For particles shown by the blue dotted line in Figure 11, the number density profile corresponds to the overdensity ρ/ρ_{mean} displayed in Figure 9, because ρ/ρ_{mean} is derived from particle distribution. The variation in number density profiles of galaxies and particles is influenced by the parameter R_s . When $R_s = 2.1 h^{-1}\text{Mpc}$, there is a notable difference between the number densities of galaxies and particles. However, at $R_s = 8.0 h^{-1}\text{Mpc}$, this difference decreases. In the case of subhaloes, their number density profile is similar to that of particles at $R_s = 2.1 h^{-1}\text{Mpc}$, but the divergence between subhaloes and particles becomes more pronounced at $R_s = 8.0 h^{-1}\text{Mpc}$.

4 SUMMARY

Using dark matter distribution from the cosmological and constrained ELUCID simulation, we have investigated the statistical properties of filaments in the cosmic web, such as the filament length distribution and the radial density profile. The cosmic web type in space is classified by the Hessian matrix of the density field. According to Equation 1, the number of eigenvalues above a certain threshold λ_{th} can be used to identify knots, filaments, sheets, and voids based on smooth density with a Gaussian filter of the smoothing scale R_s .

To study the length of the filament and the profile of the radial density, the filament axes are identified by the medial axis thinning applied in the COWS method (Pfeifer et al. 2022), based on the classifications of the cosmic web by the Hessian matrix of the density field. As shown in Figure 4, the medial axes of the filament trace the spines of cosmic filaments very well characterized by the distribution of dark-matter particles. Note that the direction of the filament can also be indicated by the eigenvector \hat{e}_3 of the density Hessian matrix in Equation 1 (Zhang et al. 2009, 2013, 2015). We confirm that the filament spines identified by the medial axis thinning algorithm are strongly aligned with the eigenvector \hat{e}_3 of the density Hessian matrix, indicating the validity of the filament finding methods.

Although the medial axis thinning algorithm has no free parameter, the cosmic web classification method has two parameters, the smoothing length R_s and the threshold λ_{th} , which can affect the statistical properties of cosmic filaments. This research mainly examines how cosmic structures are influenced by the two parameters R_s and λ_{th} . The following is a summary of our findings.

(i) The volume fraction of each type of cosmic web is strongly dependent on the threshold parameter λ_{th} . For knots, filaments, and sheets, volume fractions decrease with increasing thresholds, while the volume fraction of voids increases significantly with increasing λ_{th} . In addition, the volume fraction of each type of cosmic web is weakly dependent on the smoothing length R_s .

(ii) The filament length function varies with changes in the smoothing scales R_s . It reaches a maximum at $L \approx 2.5R_s$, from approximately $5.3 h^{-1}\text{Mpc}$ at $R_s = 2.1 h^{-1}\text{Mpc}$ to approximately $20.0 h^{-1}\text{Mpc}$ at $R_s = 8.0 h^{-1}\text{Mpc}$.

(iii) In the entire range of filament length L , the filament length functions decrease with increasing thresholds λ_{th} , demonstrating a decrease in the number of short and long filaments with increasing thresholds λ_{th} .

(iv) The PDFs of the filament lengths are strongly dependent on the smoothing scales R_s with $\log f(L) \propto L$, where $f(L)$ is the probability distribution function. The PDFs of filament lengths are very similar for different thresholds. At $R_s = 2.1 h^{-1}\text{Mpc}$, PDF can be expressed by the best-fitting relation $\log f(L) = -0.1L - 0.37$.

(v) The mass density of the filament decreases with increasing radial distance to the filament axis. The density profile of filaments exhibits an excess with respect to the mean density of the Universe.

(vi) The radial density profile of the filaments depends on the parameters R_s and λ_{th} . It reaches a valley of approximately $2R_s$. The amplitudes of the density profiles increase with increasing thresholds λ_{th} .

(vii) The radial density profiles are different for short and long filaments. Short filaments have higher density profiles than long filaments in the whole range of radial distance.

In conclusion, the results presented in this paper show that the filament length and the radial density profile depend on the smoothing scales R_s and the thresholds λ_{th} in the filament-finding method. Further analyses are useful in understanding the dependence of filament properties on the adopted parameters using different filament-finding algorithms. Using this collection of filaments derived from the ELUCID dark matter distribution, future research will explore the extraction and quantification of these filaments with respect to galaxies, utilising both the ELUCID simulation and SDSS observations in an upcoming study.

ACKNOWLEDGEMENTS

We express our gratitude to the anonymous referee for the insightful comments that greatly enhance the quality of this paper. This work is supported by the National Natural Science Foundation of China (Nos. 12273088, 11833005, 11890692, 11621303), the National Key R&D Programme of China (2023YFA1607800, 2023YFA1607804), the CSST project No. CMS-CSST-2021-A02, the Fundamental Research Funds for Central Universities, 111 project No. B20019 and the Shanghai Natural Science Foundation, grant No.19ZR1466800. PW is sponsored by the Shanghai Pujiang Programme (No. 22PJ1415100).

This work is also supported by the High-Performance Computing

Resource in the Core Facility for Advanced Research Computing at Shanghai Astronomical Observatory.

This work used *Astropy*: a community-developed core Python package and an ecosystem of tools and resources for astronomy ([Astropy Collaboration et al. 2013, 2018, 2022](#)).

Funding for the Sloan Digital Sky Survey IV has been provided by the Alfred P. Sloan Foundation, the U.S. Department of Energy Office of Science, and the Participating Institutions. SDSS acknowledges support and resources from the Centre for High-Performance Computing at the University of Utah. The SDSS website is www.sdss.org.

SDSS is managed by the Astrophysical Research Consortium for the Participating Institutions of the SDSS Collaboration including the Brazilian Participation Group, the Carnegie Institution for Science, Carnegie Mellon University, the Chilean Participation Group, the French Participation Group, Harvard-Smithsonian Center for Astrophysics, Instituto de Astrofísica de Canarias, The Johns Hopkins University, Kavli Institute for the Physics and Mathematics of the Universe (IPMU)/University of Tokyo, Lawrence Berkeley National Laboratory, Leibniz Institut für Astrophysik Potsdam (AIP), Max-Planck-Institut für Astronomie (MPIA Heidelberg), Max-Planck-Institut für Astrophysik (MPA Garching), Max-Planck-Institut für Extraterrestrische Physik (MPE), National Astronomical Observatories of China, New Mexico State University, New York University, University of Notre Dame, Observatório Nacional/ MCTI, The Ohio State University, Pennsylvania State University, Shanghai Astronomical Observatory, United Kingdom Participation Group, Universidad Nacional Autónoma de México, University of Arizona, University of Colorado Boulder, University of Oxford, University of Portsmouth, University of Utah, University of Virginia, University of Washington, University of Wisconsin, Vanderbilt University, and Yale University.

DATA AVAILABILITY

The data underlying this article will be shared on reasonable request to the corresponding author.

References

- Abazajian K. N., et al., 2009, *ApJS*, **182**, 543
 Alina D., Shomanov A., Baimukhametova S., 2022, *IEEE Access*, **10**, 74472
 Aragon-Calvo M. A., 2019, *MNRAS*, **484**, 5771
 Aragon-Calvo M. A., 2024, *MNRAS*, **529**, 74
 Aragon-Calvo M. A., Jones B. J. T., van de Weygaert R., van der Hulst J. M., 2007, *A&A*, **474**, 315
 Astropy Collaboration et al., 2013, *A&A*, **558**, A33
 Astropy Collaboration et al., 2018, *AJ*, **156**, 123
 Astropy Collaboration et al., 2022, *ApJ*, **935**, 167
 Blanton M. R., et al., 2005, *AJ*, **129**, 2562
 Bond J. R., Kofman L., Pogosyan D., 1996, *Nature*, **380**, 603
 Bond N. A., Strauss M. A., Cen R., 2010, *MNRAS*, **409**, 156
 Bonnaire T., Aghanim N., Decelle A., Douspis M., 2020, *A&A*, **637**, A18
 Buncher B., Carrasco Kind M., 2020, *MNRAS*, **497**, 5041
 Carrón Duque J., Migliaccio M., Marinucci D., Vittorio N., 2022, *A&A*, **659**, A166
 Cautun M., van de Weygaert R., Jones B. J. T., 2013, *MNRAS*, **429**, 1286
 Chen Y.-C., Ho S., Freeman P. E., Genovese C. R., Wasserman L., 2015, *MNRAS*, **454**, 1140
 Chen Y.-C., et al., 2017, *MNRAS*, **466**, 1880
 Choi E., Bond N. A., Strauss M. A., Coil A. L., Davis M., Willmer C. N. A., 2010, *MNRAS*, **406**, 320
 Colombi S., Pogosyan D., Souradeep T., 2000, *Phys. Rev. Lett.*, **85**, 5515
 DESI Collaboration et al., 2024, *AJ*, **168**, 58
 Diemer B., Kravtsov A. V., 2014, *ApJ*, **789**, 1

- Dubois Y., et al., 2014, *MNRAS*, **444**, 1453
 Forero-Romero J. E., Hoffman Y., Gottlöber S., Klypin A., Yepes G., 2009, *MNRAS*, **396**, 1815
 Galárraga-Espinosa D., Aghanim N., Langer M., Gouin C., Malavasi N., 2020, *A&A*, **641**, A173
 Galárraga-Espinosa D., et al., 2024, *A&A*, **684**, A63
 Hahn O., Porciani C., Carollo C. M., Dekel A., 2007, *MNRAS*, **375**, 489
 Hernández-Aguayo C., et al., 2023, *MNRAS*, **524**, 2556
 Hoffman Y., Metuki O., Yepes G., Gottlöber S., Forero-Romero J. E., Libeskind N. I., Knebe A., 2012, *MNRAS*, **425**, 2049
 Inoue S., Si X., Okamoto T., Nishigaki M., 2022, *MNRAS*, **515**, 4065
 Kraljic K., et al., 2018, *MNRAS*, **474**, 547
 Kuutma T., Tamm A., Tempel E., 2017, *A&A*, **600**, L6
 Laigle C., et al., 2018, *MNRAS*, **474**, 5437
 Lee T., Kashyap R., Chu C., 1994, *CVGIP: Graphical Models and Image Processing*, **56**, 462
 Libeskind N. I., et al., 2018, *MNRAS*, **473**, 1195
 Malavasi N., et al., 2017, *MNRAS*, **465**, 3817
 Malavasi N., Aghanim N., Douspis M., Tanimura H., Bonjean V., 2020, *A&A*, **642**, A19
 Martínez H. J., Muriel H., Coenda V., 2016, *MNRAS*, **455**, 127
 Peebles P. J. E., 1967, *ApJ*, **147**, 859
 Pereyra L. A., Sgró M. A., Merchán M. E., Stasyszyn F. A., Paz D. J., 2020, *MNRAS*, **499**, 4876
 Pfeifer S., Libeskind N. I., Hoffman Y., Hellwing W. A., Bilicki M., Naidoo K., 2022, *MNRAS*, **514**, 470
 Rost A., Stasyszyn F., Pereyra L., Martínez H. J., 2020, *MNRAS*, **493**, 1936
 Sousbie T., 2011, *MNRAS*, **414**, 350
 Sousbie T., Pichon C., Kawahara H., 2011, *MNRAS*, **414**, 384
 Springel V., 2005, *MNRAS*, **364**, 1105
 Springel V., et al., 2005, *Nature*, **435**, 629
 Stoica R. S., Martínez V. J., Mateu J., Saar E., 2005, *A&A*, **434**, 423
 Suárez-Pérez J. F., Camargo Y., Li X.-D., Forero-Romero J. E., 2021, *ApJ*, **922**, 204
 Tempel E., Stoica R. S., Martínez V. J., Liivamägi L. J., Castellan G., Saar E., 2014, *MNRAS*, **438**, 3465
 Wang H., Mo H. J., Yang X., Jing Y. P., Lin W. P., 2014, *ApJ*, **794**, 94
 Wang H., et al., 2016, *ApJ*, **831**, 164
 Wang H., et al., 2018, *ApJ*, **852**, 31
 Wang P., Kang X., Libeskind N. I., Guo Q., Gottlöber S., Wang W., 2020, *New Astron.*, **80**, 101405
 Wang W., et al., 2024a, *arXiv e-prints*, p. arXiv:2402.11678
 Wang Z., Shi F., Yang X., Li Q., Liu Y., Li X., 2024b, *Science China Physics, Mechanics, and Astronomy*, **67**, 219513
 Winkel N., Pasquali A., Kraljic K., Smith R., Gallazzi A., Jackson T. M., 2021, *MNRAS*, **505**, 4920
 Yang X., Mo H. J., van den Bosch F. C., Pasquali A., Li C., Barden M., 2007, *ApJ*, **671**, 153
 Yang X., Mo H. J., van den Bosch F. C., Zhang Y., Han J., 2012, *ApJ*, **752**, 41
 Yang X., et al., 2018, *ApJ*, **860**, 30
 Yang T., Hudson M. J., Afshordi N., 2022, *MNRAS*, **516**, 6041
 Zakharaova D., Vulcani B., De Lucia G., Xie L., Hirschmann M., Fontanot F., 2023, *MNRAS*, **525**, 4079
 Zel'dovich Y. B., 1970, *A&A*, **5**, 84
 Zhang T. Y., Suen C. Y., 1984, *Commun. ACM*, **27**, 236–239
 Zhang Y., Yang X., Faltenbacher A., Springel V., Lin W., Wang H., 2009, *ApJ*, **706**, 747
 Zhang Y., Yang X., Wang H., Wang L., Mo H. J., van den Bosch F. C., 2013, *ApJ*, **779**, 160
 Zhang Y., Yang X., Wang H., Wang L., Luo W., Mo H. J., van den Bosch F. C., 2015, *ApJ*, **798**, 17
 Zhang Y., Yang X., Guo H., 2021a, *MNRAS*, **500**, 1895
 Zhang Y., Yang X., Guo H., 2021b, *MNRAS*, **507**, 5320
 Zhang Y., de Souza R. S., Chen Y.-C., 2022a, *MNRAS*, **517**, 1197
 Zhang Y., Yang X., Guo H., 2022b, *MNRAS*, **517**, 3579
 de Lapparent V., Geller M. J., Huchra J. P., 1986, *ApJ*, **302**, L1

This paper has been typeset from a \TeX/L\AA\TeX file prepared by the author.